Earth-Moon Orbit Design for a Rapid-Response Asteroid Interceptor System

Alessandro Massini(1)(2), Noelle Elisabeth May(2), Moacir Fonseca Becker(2), Andrea Capannolo(2)

(1)*Department of Aerospace Science and Technology, Politecnico di Milano*
Milan, Italy
Email: alessandro.massini@mail.polimi.it

(2)*School of Aeronautics and Astronautics, Purdue University*
West Lafayette, Indiana, USA
Email: nemay@purdue.edu, mfonsec@purdue.edu, acapa@purdue.edu

Abstract – **Potentially hazardous objects (PHOs) represent a significant natural threat to Earth, particularly in late-warning scenarios where detection occurs only months or a few years before a possible impact. Since conventional reactive missions may require several years, pre-deployed kinetic impactors on suitable Earth–Moon parking orbits offer a promising alternative, enabling rapid departure once a hazardous object is identified. This work investigates candidate periodic orbits in the Earth–Moon system and optimizes bi-impulsive escape transfers for such a pre-deployed impactor. The dynamics are modeled in the Circular Restricted Three-Body Problem, and escape trajectories are optimized and propagated up to a switching surface (SW). The resulting departure conditions are then patched with heliocentric transfers toward two fictitious PHOs, introduced as representative test cases. Patching is enforced in terms of epoch and outgoing velocity and position at the SW. Overall, the study assesses Earth–Moon parking orbits and bi-impulsive escape paths for pre-deployed kinetic impactors, highlighting trade-offs between departure efficiency, station-keeping cost, and reachability of representative fictitious PHAs under constrained time and propellant budgets.**

I. INTRODUCTION

Modern planetary-defense efforts began in the early 1990s with the Spaceguard Survey, formalizing the need for systematic discovery and cataloging of near-Earth objects (NEOs) as a first step toward impact mitigation [1]. Among the overall NEO population, potentially hazardous objects (PHOs) represent a major concern for planetary-defense applications, due to their close orbital approaches to Earth and sizes capable of causing severe effects in case of impact [2]. Despite the significant progress achieved by current survey programs, the known NEO population remains incomplete, with recent estimates indicating a completeness of only about 38% for the objects of interest [3].

Among current planetary-defense techniques, NASA's Double Asteroid Redirection Test (DART) demonstrated the viability of the kinetic-impactor approach by altering the orbital motion of a small asteroid through a high-velocity spacecraft impact. However, its practical effectiveness relies on sufficient warning time, as mission design and deflection prediction may require several years, preferably decades [4]; moreover, for larger objects, the effectiveness of a single Earth-launched impactor is limited by launch-capability mass constraints. Consequently, in late-discovery scenarios, where a PHO on an Earth-impacting trajectory is discovered only a few years or months before the impact, kinetic-impactor strategies, as conventionally conceived, may not provide sufficient response time. This motivates the investigation of architectures in which part of the response capability is prepared before the threat is identified.

One promising option is to pre-deploy one or more kinetic impactors in the Earth–Moon environment and keep them in a long-term parking orbit, ready to rapidly leave the system once a hazardous object is detected. In this context, an effective staging orbit should combine favorable stability properties with accessible escape opportunities, allowing the spacecraft to remain on orbit for an unknown amount of time with the lowest possible station-keeping cost, while still being able to efficiently leave the Earth–Moon system to intercept the threat. Therefore, the problem consists not only in the design of the heliocentric leg to the asteroid, but also in its integration with the selection of a suitable parking orbit and the optimization of the associated escape trajectory.

Previous studies have already analyzed the possibility to exploit the lunar and cislunar environments for planetary-defense outposts [5–7] as well as the concept of parking a spacecraft while waiting for an unknown target to be intercepted [8]. However these works generally focus on prescribed locations or specific orbits, selected according to particular mission needs and constraints, and a systematic comparison of multiple staging orbits remains largely unexplored.

The present work addresses this gap by proposing a preliminary workflow to compare candidate Earth–Moon parking orbits for pre-deployed kinetic impactors, accounting for both long-term parking capability and escape opportunities. For each candidate orbit, a bi-impulsive Earth–Moon escape is optimized and propagated up to a switching surface (SW), where it is patched with a heliocentric transfer toward a selected hazardous object. The heliocentric leg is designed to provide a kinetic impact that maximizes the asteroid displacement at the subsequent Earth close approach.

The paper is organized as follows. Section II introduces the adopted dynamical framework. Section III describes the computational approach used for orbit generation, escape optimization, and heliocentric patching. The main results are presented and discussed in Section IV, while Section V summarizes the conclusions and possible future developments.

II. DYNAMICAL FRAMEWORK

In this section, the dynamical models used in the work are introduced.

A. *Circular Restricted Three-Body Problem*

The Earth–Moon dynamics are modeled through the Circular Restricted Three-Body Problem (CR3BP), in which the Earth and Moon, called the primaries, are assumed to move in circular and coplanar orbits around their common barycenter, while the spacecraft is considered to be massless and its motion to be governed only by the primaries' gravitational attraction. The equations of motion are conveniently formulated in non-dimensional form with respect to a rotating reference frame centered at the Earth–Moon barycenter [9]. The scaling quantities of the system are reported in Table 1. The x-axis of the frame is oriented along the line from the Earth to the Moon, the z-axis is orthogonal to the orbital plane of the primaries and the y-axis completes the right-handed triad.

Let the state vector be denoted by $\boldsymbol{x} \in \mathbb{R}^6$, expressed in Cartesian coordinates and containing the spacecraft position and velocity, the equations of motion can be written as $\dot{\boldsymbol{x}} = \boldsymbol{f}(\boldsymbol{x})$, with:

$$\boldsymbol{f}(\boldsymbol{x}) = \begin{bmatrix} \boldsymbol{v} \\ \boldsymbol{a}(\boldsymbol{x}) \end{bmatrix}, \quad \boldsymbol{a}(\boldsymbol{x}) = \begin{bmatrix} 2\dot{y} + \dfrac{\partial \Omega}{\partial x} \\ -2\dot{x} + \dfrac{\partial \Omega}{\partial y} \\ \dfrac{\partial \Omega}{\partial z} \end{bmatrix}. \tag{1}$$

Here, Ω represents the pseudo-potential function and is defined as:

$$\Omega(x, y, z) = \frac{1}{2}(x^2 + y^2) + \frac{1-\mu}{r_1} + \frac{\mu}{r_2}, \tag{2}$$

where

$$r_1 = \sqrt{(x+\mu)^2 + y^2 + z^2}, \tag{3a}$$

$$r_2 = \sqrt{(x-1+\mu)^2 + y^2 + z^2}, \tag{3b}$$

$$\mu = \frac{m_2}{m_1 + m_2} \tag{3c}$$

and m_1 and m_2 are the masses of the Earth and Moon, respectively.

Table 1. Parameters in Earth–Moon System

Earth–Moon CRTBP parameters	
Length unit [km]	385692.5
Time unit [s]	377084.2
Earth gravitational parameter [km^3/s^2]	398600.4
Moon gravitational parameter [km^3/s^2]	4902.80
Mass ratio of Earth–Moon system [-]	0.012151
Earth radius [km]	6371
Moon radius [km]	1737

B. *Switching Surface*

The CR3BP is adopted to model the spacecraft dynamics within the Earth–Moon region. However, since asteroid interception requires a heliocentric transfer, an interface between the Earth–Moon escape arc and the heliocentric leg must be introduced.

Although the transition between Earth–Moon and heliocentric dynamics is continuous, a finite switching boundary must be defined. In patched-conic approaches, the Earth sphere of influence provides a practical surface for this transition. Here, a larger switching surface is adopted to define the interface in a region where the transition to the heliocentric model is less sensitive to local Earth–Moon dynamics. Specifically, the SW is modeled as an Earth-centered sphere with radius $R_{\text{SW}} = 2 \times 10^6$ km, approximately twice the classical Earth SOI radius, following the approach adopted in [10].

C. *Heliocentric Dynamics*

Beyond the switching surface the motion of both the kinetic-impactor and the asteroid is modeled through a heliocentric two-body problem (2BP). The heliocentric states are expressed in the Sun-centered ECLIPJ2000 inertial frame, whose fundamental plane is the mean ecliptic plane at the J2000 epoch, with the x-axis pointing toward the J2000 vernal equinox and the z-axis aligned with the north ecliptic pole. The Sun is assumed to be the only attracting body and all other masses are considered negligible. Under this assumption, the motion of a generic body is described by

$$\ddot{\boldsymbol{r}} = -\mu_\odot \frac{\boldsymbol{r}}{\|\boldsymbol{r}\|^3}, \tag{4}$$

where $\boldsymbol{r}$ is the heliocentric position vector and $\mu_\odot$ is the solar gravitational parameter. A more detailed treatment of the 2BP can be found in [11].

III. METHODOLOGY

This section presents the methodology adopted in this work. The first part describes the generation of the parking periodic orbits and the metric used to evaluate their storage capabilities, while the second part focuses on the optimization of the escape trajectories from the Earth–Moon system, on its associated performance indicators and on the adopted patching procedure. Finally, the third part introduces the heliocentric trajectory design toward two fictitious hazardous-objects as test cases and defines the kinetic impact model used to model the interception.

A. Orbits Generation and Assessment

In the CR3BP, a periodic orbit is a solution whose state repeats itself after a finite period T, i.e,

$$\boldsymbol{x}(t+T) = \boldsymbol{x}(t), \qquad T > 0, \tag{5}$$

where $\boldsymbol{x} = [x, y, z, \dot{x}, \dot{y}, \dot{z}]^\top$ is the spacecraft state in the rotating frame [12]. The numerical techniques used to compute periodic solutions and to continue them into families are extensively investigated in previous works [13]. In this work, a full-state multivariate Newton method combined with a single-shooting formulation is adopted to enforce periodicity.

Let $\boldsymbol{X} \in \mathbb{R}^{n\times 1}$ be the column vector of free variables and $\boldsymbol{F}(\boldsymbol{X}) \in \mathbb{R}^{m\times 1}$ the corresponding constraints vector. The objective of the correction scheme is to drive the constraints residuals to zero, namely

$$\boldsymbol{F}(\boldsymbol{X}) = \boldsymbol{0}. \tag{6}$$

At the k-th iteration, the design-variable vector is updated through a Newton correction based on the constraints Jacobian

$$\boldsymbol{X}_{k+1} = \boldsymbol{X}_k - D\boldsymbol{F}(\boldsymbol{X}_k)^\dagger \boldsymbol{F}(\boldsymbol{X}_k), \tag{7}$$

where $\boldsymbol{X}_k$ is the vector of free variables at k-th iteration, $\boldsymbol{F}(\boldsymbol{X}_k)$ is the corresponding vector of residual constraint, $D\boldsymbol{F}(\boldsymbol{X}_k)$ is the Jacobian matrix of the constraints with respect to the free variables and the symbol $(\cdot)^\dagger$ denotes the Moore-Penrose pseudoinverse. The vector $\boldsymbol{X}_{k+1}$ is the corrected solution obtained after the Newton update [9].

In this work, the free-variable vector includes the full initial state and the orbital period T, while the constraints vector enforces the equality between the propagated final state after one period and the initial state,

$$\boldsymbol{X} = \begin{bmatrix} x_0 \\ y_0 \\ z_0 \\ \dot{x}_0 \\ \dot{y}_0 \\ \dot{z}_0 \\ T \end{bmatrix} \quad ; \quad \boldsymbol{F}(\boldsymbol{X}) = \begin{bmatrix} x(T) - x_0 \\ y(T) - y_0 \\ z(T) - z_0 \\ \dot{x}(T) - \dot{x}_0 \\ \dot{y}(T) - \dot{y}_0 \\ \dot{z}(T) - \dot{z}_0 \\ \psi(\boldsymbol{X}) \end{bmatrix}. \tag{8}$$

Here, $\psi(\boldsymbol{X})$ represents a phase condition, imposed by fixing one initial-state component to a prescribed value. This additional condition is required because the periodicity equations alone do not isolate a unique solution: they are invariant under a shift along the orbit or along the family. The phase condition therefore fixes a unique representative point on the orbit.

The remaining degree of freedom along the family is handled through pseudo-arclength continuation [14]. This condition both advances the solution along the family and selects a unique next member by prescribing its arclength distance from the previous orbit. At each converged solution $\boldsymbol{X}_{k-1}$, the tangent direction to the solution branch, namely $\Delta\boldsymbol{X}_{k-1}$, is obtained from the nullspace of $D\boldsymbol{F}(\boldsymbol{X}_{k-1})$. A predictor solution is then generated by moving a prescribed arclength step Δs along the tangent direction. The predicted solution is subsequently refined using the Newton differential-correction scheme described in (7). The constraint vector, and the associated Jacobian matrix, are augmented such that the new solution $\boldsymbol{X}_k$ is forced to be shifted by a stepsize Δs along the tangent direction:

$$\boldsymbol{G}(\boldsymbol{X}_k) = \begin{bmatrix} \boldsymbol{F}(\boldsymbol{X}_k) \\ (\boldsymbol{X}_k - \boldsymbol{X}_{k-1})^\top \Delta\boldsymbol{X}_{k-1} - \Delta s \end{bmatrix}, \tag{9a}$$

$$D\boldsymbol{G}(\boldsymbol{X}_{\boldsymbol{k}}) = \begin{bmatrix} D\boldsymbol{F}(\boldsymbol{X}_k) \\ \Delta\boldsymbol{X}_{k-1}^\top \end{bmatrix}. \tag{9b}$$

Stationkeeping Analysis. The long-term parking capability of each periodic orbit is assessed through a Floquet-based stationkeeping strategy, whose objective is to remove the unstable components of the deviation expressed in the Floquet reference frame [15]. The time-varying Floquet basis is constructed by propagating the eigenvectors ($\boldsymbol{V_0}$) of the monodromy matrix along the nominal orbit,

$$\boldsymbol{E}(t) = \boldsymbol{\Phi}(t, 0)\boldsymbol{V}_0. \tag{10}$$

The projection matrix onto the Floquet coordinates is then given by $\boldsymbol{P}(t) = \boldsymbol{E}^{-1}(t)$. At the k-th control epoch, the deviation from the reference trajectory, $\delta\boldsymbol{x}_k$, is defined as the difference between the actual spacecraft state and its local nearest reference point [16], and is projected onto the unstable subspace as

$$\boldsymbol{c}_u(t_k) = \boldsymbol{P}_u(t_k)\delta\boldsymbol{x}_k, \tag{11}$$

where $\boldsymbol{P}_u(t_k)$ contains the rows of $\boldsymbol{P}(t_k)$ associated with the unstable modes. The correction maneuver is designed to remove the projected unstable component. Since only the velocity is modified, the resulting minimum-norm impulse is

$$\Delta\boldsymbol{v}_k = -\boldsymbol{P}^\dagger_{u,v}(t_k)\boldsymbol{c}_u(t_k), \tag{12}$$

where $\boldsymbol{P}_{u,v}$ is the velocity block of $\boldsymbol{P}_u$.

For each candidate orbit, the annual stationkeeping cost is assessed through a Monte Carlo simulation with 1000 samples. Control opportunities are scheduled at fixed 7-day intervals. The analysis includes initial orbit insertion errors, modeled as zero-mean Gaussian dispersions with standard deviations $\sigma_r = 2$ km in position and $\sigma_v = 1$ cm/s in velocity [15], and maneuver execution errors, modeled as a 5% relative vector error [16] plus a 10^{-5}

m/s absolute error. State-estimation errors are neglected for simplicity, and the spacecraft state is assumed to be perfectly known at each correction epoch.

B. Bi-Impulsive Escape Optimization

For each parking orbit considered in this work, a bi-impulsive escape trajectory is optimized to reach a prescribed outgoing velocity $\boldsymbol{v}_\infty$ at the switching surface. In the following, $\boldsymbol{v}_\infty$ is used in a patched-conic sense to denote the outgoing geocentric velocity at this surface, rather than a true two-body hyperbolic excess velocity.

A bi-impulsive strategy is adopted: the first maneuver is performed along the parking orbit to target a close Earth passage, while the second maneuver is applied near perigee to exploit the Oberth effect [17] and provide the final velocity increment required for escape.

This strategy is selected as a trade-off between single-impulse transfers, which allow fast departures but concentrate the required velocity increment in one maneuver, and lower-energy escape mechanisms exploiting weak stability boundary (WSB) regions and solar perturbations, which typically involve longer transfer times and a larger design space. More complex maneuvered mechanisms, such as reversed-WSB escapes with a perigee maneuver, may improve the escape efficiency but are left for future work. The reader is referred to [6] for a comprehensive classification of escape strategies.

The escape design is carried out through a two-step procedure. First, a preliminary grid search is performed on the selected orbits to identify suitable initial guesses that lead to a close Earth passage and provide outgoing conditions at the switching surface sufficiently close to the target values, both in terms of position and velocity. Then, the best candidates obtained from this preliminary step are refined through a nonlinear programming (NLP) optimization.

Grid Search. The grid search is designed to identify feasible escape trajectories and provide a suitable initial guess for the subsequent NLP optimization. The sampled variables are the pseudo-mean anomaly S, which identifies the departure point along the parking orbit, the magnitude of the first maneuver Δv_1, and two angles, α and β, which define its direction as

$$\Delta \boldsymbol{v}_1 = \Delta v_1 \begin{bmatrix} \cos\beta \sin\alpha \\ \cos\beta\cos\alpha \\ \sin\beta \end{bmatrix}. \tag{13}$$

The pseudo-mean anomaly is introduced to distribute the sampled departure points uniformly along the orbit arc length and it is defined as

$$S(\tau) = 2\pi \frac{s(\tau)}{s(1)}, \tag{14}$$

where $\tau = t/T$, T is the orbital period, and

$$s(\tau) = \int_0^\tau |\dot{\boldsymbol{r}}(u)|\, du \qquad \text{with} \qquad \tau \in [0, 1). \tag{15}$$

For each grid point, the trajectory is propagated until one of the following events is detected: Earth impact, Moon impact, close Earth perigee, direct escape, or maximum propagation time. Only trajectories reaching an Earth perigee are retained, while all other cases are discarded. At perigee, a second tangential maneuver is applied. For computational reasons, the magnitude of this maneuver is fixed according to the prescribed outgoing target velocity. Finally, the trajectory is propagated up to the switching surface, where three figures of merit are used to assess the quality of the candidate trajectory [6]:

$$\delta_v = \left| 1 - \frac{v_\infty^+}{v_\infty^-} \right|, \tag{16a}$$

$$\eta_r = \arccos\left(\frac{\boldsymbol{r}^+ \cdot \boldsymbol{r}^-(\theta_m)}{r^+ r^-(\theta_m)} \right), \tag{16b}$$

$$\eta_v = \arccos\left(\frac{\boldsymbol{v}^+ \cdot \boldsymbol{v}^-(\theta_m)}{v^+ v^-(\theta_m)} \right). \tag{16c}$$

Here, the superscripts $+$ and $-$ denote the target and achieved quantities at the switching surface, respectively. The angle θ_m represents the orientation between the synodic reference frame and the ECLIPJ2000 frame at the patching epoch.

Optimization Problem Formulation. The trajectory is refined by means of a constrained nonlinear optimization procedure in order to enforce the required patching conditions with higher accuracy. The problem is written in compact form as

$$\begin{aligned} \min_{\boldsymbol{x}} \quad & J(\boldsymbol{x}) \\ \text{subject to} \quad & \boldsymbol{c}_{\text{eq}}(\boldsymbol{x}) = \boldsymbol{0}, \\ & \boldsymbol{c}_{\text{ineq}}(\boldsymbol{x}) \leq \boldsymbol{0}, \\ & \boldsymbol{x}_{\text{lb}} \leq \boldsymbol{x} \leq \boldsymbol{x}_{\text{ub}}, \end{aligned} \tag{17}$$

where $\boldsymbol{x}$ collects the design variables, J is the objective function, and $\boldsymbol{c}_{\text{eq}}$ and $\boldsymbol{c}_{\text{ineq}}$ denote the equality and inequality constraints, respectively.

As design variables for the optimization, the following set is adopted:

$$\boldsymbol{x} = \left[\theta_1, \Delta v_{x1}, \Delta v_{y1}, \Delta v_{z1}, t_{fb}, \Delta v_{x2}, \Delta v_{y2}, \Delta v_{z2}, t_f\right]^\top, \tag{18}$$

where θ_1 is the departure phase along the parking orbit. The subscripts $(\cdot)_1$ and $(\cdot)_2$ refer to the first and second maneuvers, respectively. The variable t_{fb} denotes the time where the second maneuver is applied, while t_f is the final time at which the trajectory reaches the switching surface.

The objective function accounts for the two main performance indicators considered in this work: the maneuvering cost and the total time of flight. It is defined as

$$J(\boldsymbol{x}) = \lambda_1 \left(\|\Delta \boldsymbol{v}_1\| + \|\Delta \boldsymbol{v}_2\| \right) + \lambda_2 t_{tot}, \tag{19}$$

with λ_1 and λ_2 two weighting coefficients.

The constraints imposed in the optimization include both terminal patching conditions and continuous-time collision-avoidance requirements. The former ensure consistency with the prescribed heliocentric departure state at the switching surface, while the latter enforce safe clearance from the primaries along the entire escape trajectory, as summarized below.

1) *Patching constraints.* These constraints enforce the compatibility between the optimized escape trajectory and the target outgoing conditions at the switching surface. Since this analysis is intended as a preliminary design step for subsequent higher-fidelity refinements, only the switching-surface distance is imposed as an equality constraint. The velocity-magnitude error and the angular errors in position and velocity are instead bounded by prescribed tolerances:

$$r_f - r_{\mathrm{SW}} = 0, \tag{20a}$$

$$\delta_v \leq 0.01, \tag{20b}$$

$$\eta_v \leq 5^\circ, \tag{20c}$$

$$\eta_r \leq 5^\circ. \tag{20d}$$

2) *Continuous-time Collision Avoidance.* To guarantee a safe distance from the primaries along the entire trajectory, collision-avoidance constraints are imposed with respect to both the Earth and the Moon. A simple discrete formulation would require,

$$r_{\min,p} \leq \|\boldsymbol{r}_k - \boldsymbol{r}_{p,k}\|, \qquad k \in 1,\ldots,N, \tag{21}$$

where N are the discretization nodes of the trajectory and $p \in \{\oplus, M\}$ denotes the primary. However, enforcing this condition only at discrete points does not guarantee collision avoidance between consecutive nodes. Therefore, following the continuous-time formulation of [18], the safety condition is imposed as

$$\|\boldsymbol{r}(t) - \boldsymbol{r}_p(t)\| - r_{\min,p} \geq 0, \qquad \forall t. \tag{22}$$

To embed this condition into the trajectory propagation, a smooth per-primary penalty is introduced as a differentiable approximation of the positive-part violation:

$$\Lambda_p(\boldsymbol{r}) = \left[\frac{1}{\alpha}\log\left(1 + e^{\alpha\left[1 - \frac{\|\boldsymbol{r}-\boldsymbol{r}_p\|}{r_{\min,p}}\right]}\right)\right]^{n_\lambda}. \tag{23}$$

Here, α controls the sharpness of the smooth approximation, while $n > 1$ is the penalty exponent.

The original penalty used in [18] is replaced in this work to improve differentiability within the gradient-based optimization.

The dynamical system is then augmented with two additional states which collect the time integrals of the collision-avoidance penalties:

$$\boldsymbol{q} = \begin{bmatrix} q_\oplus \\ q_M \end{bmatrix}, \qquad \dot{\boldsymbol{q}} = \begin{bmatrix} \Lambda_\oplus \\ \Lambda_M \end{bmatrix}, \qquad \boldsymbol{q}(0) = \boldsymbol{0}. \tag{24}$$

The continuous-time collision-avoidance condition is finally enforced by imposing

$$\boldsymbol{q}(t_f) = \boldsymbol{0}. \tag{25}$$

Since each penalty term is non-negative, this terminal condition is equivalent to requiring the integral of the violation to vanish, thus enforcing the safety condition over the full trajectory. The minimum allowable altitudes are set to $h_{\min,\oplus} = 2000$ km and $h_{\min,M} = 500$ km for Earth and Moon, respectively.

The resulting problem in (17) is solved using the MATLAB `fmincon` function with the `sqp` algorithm. Analytical gradients are supplied for the objective function and all nonlinear constraints to improve convergence robustness and computational efficiency.

C. Heliocentric Leg Definition

The heliocentric leg is introduced to assess the capability of the escape conditions of being connected to a trajectory intercepting a hazardous object .

Since a full reachability map of the existing PHO population would require a significant computational effort, two fictitious hazardous objects are generated to reproduce heliocentric trajectories impacting with Earth.

Starting from an impact with Earth set to November 12th, 2040 the heliocentric orbital parameters of Earth are modified in order to obtain two trajectories with different semi-major axis, eccentricity and inclination characteristics. Table 2 summarizes the resulting orbital elements.

The heliocentric transfers are designed in Sun-centered two-body dynamics by means of a grid search over the departure epoch at the switching surface and the asteroid interception epoch. For each pair of dates, a Lambert arc is computed and the corresponding outgoing velocity at the switching surface is evaluated [19]. Since the transfer aims at minimizing the required outgoing velocity magnitude and maximizing the asteroid deviation at the Earth close-approach epoch, the set of grid-search solutions is analyzed in a Pareto optimality sense [20]. The best solution is selected as the Pareto candidate closest to the utopia point, defined as

$$\boldsymbol{z}^\star = \begin{bmatrix} v_\infty^{\min} & \Delta r^{\max} \end{bmatrix}^\top. \tag{26}$$

Leg Optimization. Once a suitable initial guess is selected, the heliocentric leg is refined through a nonlinear optimization problem, formulated in the general form of (17). Specifically, the optimization aims to minimize the required outgoing velocity magnitude v_∞ at the switching surface, while ensuring that the kinetic impact (KI) produces at least a prescribed displacement of the asteroid at its Earth close approach.

Table 2. Keplerian elements for the hazardous objects

ID	$\boldsymbol{a}$ [AU]	$\boldsymbol{e}$ [-]	$\boldsymbol{i}$ [°]	$\boldsymbol{\Omega}$ [°]	$\boldsymbol{\omega}$ [°]	$\boldsymbol{\theta}$ [°]
1	1.046	0.3912	2.024	50.22	105.6	254.4
2	1.635	0.5185	6.984	50.22	66.41	293.6

This choice does not directly minimize the Earth–Moon escape Δv, but it provides a preliminary criterion since v_∞ represents the target outgoing condition to be matched by the escape leg. The design variables are defined as follows

$$\boldsymbol{x} = \begin{bmatrix} \theta & \delta & \alpha & \beta & v_\infty & \Delta t_0 & \Delta t_f \end{bmatrix}^\top, \tag{27}$$

where θ and δ define the longitude and declination of the spacecraft position at the switching surface in the Earth-inertial J2000 frame, while α and β define the direction of the outgoing velocity $\boldsymbol{v}_\infty$ in the same frame, consistently with the parametrization introduced in (13). Finally, Δt_0 and Δt_f are the time shifts applied to the departure and interception epochs with respect to the initial guess.

Two mission constraints are imposed on the heliocentric transfer. The first enforces the interception of the asteroid at the impact epoch, while the second requires the post-impact asteroid trajectory to achieve a minimum displacement from Earth at the close-approach epoch:

$$\boldsymbol{r}_{\text{sc}}(t_f) - \boldsymbol{r}_A(t_f) = \boldsymbol{0}, \tag{28a}$$

$$d_{\text{min}} - \left\| \boldsymbol{r}_A^+(t_{\text{CA}}) - \boldsymbol{r}_\oplus(t_{\text{CA}}) \right\| \leq 0, \tag{28b}$$

where the $+$ superscript denotes the modified asteroid trajectory after the kinetic impact.

Finally, the objective function is defined as the squared magnitude of the required outgoing velocity at the switching surface:

$$J(\boldsymbol{x}) = v_\infty^2. \tag{29}$$

Kinetic Impact Model. The kinetic impact is modeled as an inelastic collision between the spacecraft and the asteroid. To account for the additional momentum transfer produced by ejecta during crater formation, a momentum-transfer efficiency factor β is introduced. Following [21], $\beta = 3.6$ is adopted, consistently with DART-like results. The velocity variation imparted to the asteroid is computed from momentum conservation as

$$\Delta \boldsymbol{v}_A = \beta \frac{m}{m+M} \left(\boldsymbol{v}_{\text{SC}} - \boldsymbol{v}_A \right), \tag{30}$$

where $\boldsymbol{v}_{\text{SC}} - \boldsymbol{v}_A$ is the spacecraft velocity relative to the asteroid at interception, and m and M are the spacecraft and asteroid masses, respectively. Assuming a spherical asteroid with density $\rho_A = 2500\ \text{kg/m}^3$ and diameter D, the asteroid mass is computed as

$$M = \rho_A \frac{\pi D^3}{6}. \tag{31}$$

IV. NUMERICAL RESULTS

This section presents the numerical results of the proposed methodology. First, two representative candidate orbits are introduced among the analyzed families, together with their stationkeeping performance. Then, the corresponding escape trajectories are assessed in terms of maneuvering cost, time of flight, and compatibility with the heliocentric transfers. Finally, the resulting asteroid deviations are discussed for the considered fictitious hazardous objects.

A. Orbits and Stationkeeping Results

Two resonant periodic orbits, belonging to the 2:1 and 3:1 families, are selected as representative test cases for the proposed methodology. At this stage, the objective is not to identify globally optimal staging solutions, but rather to assess the complete workflow on two dynamically distinct and representative cases. Within each family, one orbit is retained as a representative test case. The initial conditions of the selected orbits are reported in the synodic frame in non dimensional units in Table 3.

The stationkeeping performance of the two selected orbits is then evaluated through the Monte Carlo procedure described in Section III, and the main results are summarized in Table 4. The results indicate that both selected orbits exhibit sustainable annual stationkeeping costs. However, the resonant 2:1 orbit requires a significantly lower annual propellant budget. The larger dispersion observed for the 3:1 case suggests that its required correction effort is more sensitive to the direction of the initial perturbation and to its projection onto the unstable Floquet modes. Conversely, the 2:1 orbit shows a more repeatable behavior across the Monte Carlo campaign, making it the more suitable candidate for long-term storage from a stationkeeping standpoint.

Fig. 1 and Fig. 2 show the nominal and controlled trajectories for the two selected resonant orbits in the rotating system. The grey curves correspond to missed-thrust-event (MTE) trajectories, obtained by propagating selected pre-maneuver states without applying the sched-

Table 3. Initial conditions for the candidate orbits.

Orbit	$\boldsymbol{x}$	$\boldsymbol{y}$	$\boldsymbol{z}$	$\boldsymbol{v_x}$	$\boldsymbol{v_y}$	$\boldsymbol{v_z}$
3:1	0.0537745	0	0	0	5.2106193	0
2:1	1.0685367	0	0	0	-0.8218546	0

Table 4. One-year stationkeeping performance.

Metric	**3:1**	**2:1**
Mean Δv_{cmd} [m/s per year]	16.738	0.92878
Median Δv_{cmd} [m/s per year]	11.996	0.87501
Std. dev. Δv_{cmd} [m/s per year]	15.202	0.37913
Mean max. position error [km]	1838.85	267.567
Std. max. position error [km]	1414.26	39.44

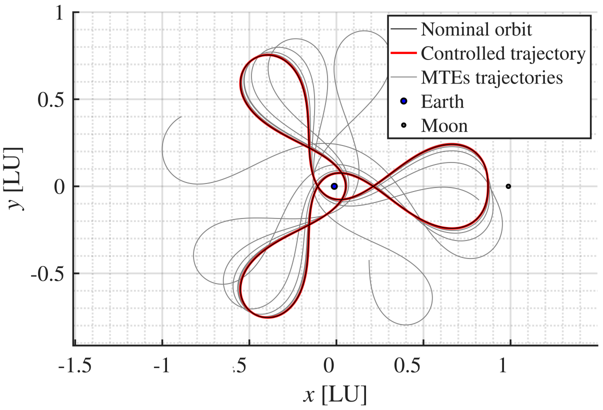

Fig. 1: *Resonant 3:1 nominal and controlled orbit.*

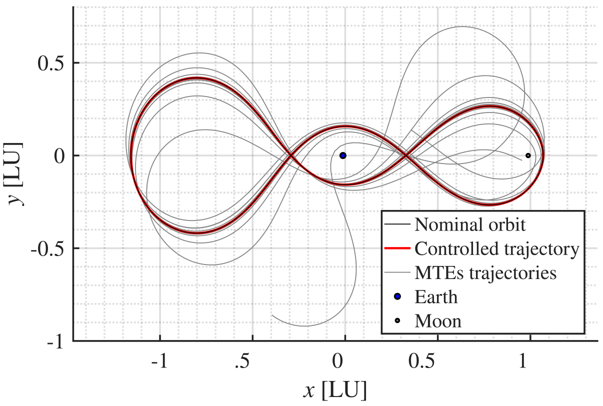

Fig. 2: *Resonant 2:1 nominal and controlled orbit.*

uled stationkeeping correction. For visualization purposes, the MTE trajectories are propagated for 80 days in the 3:1 case and 150 days in the 2:1 case and they illustrate the natural divergence from the nominal orbit in the absence of stationkeeping control.

B. *Escape and Asteroid Interception*

The previous section assessed the long-term parking capability of the two selected resonant orbits. The next step is to determine whether these parking orbits can provide suitable departure conditions for asteroid interception. Therefore, this section first presents the optimized heliocentric transfers and then evaluates the ability of each Earth–Moon escape trajectory to match the corresponding departure conditions at the switching surface.

In the present test case, two fictitious hazardous objects with diameter $D = 80$ m are considered. The earliest allowable departure from the switching surface is set to June 1st, 2035, while the latest allowable asteroid-interception epoch is October 31st, 2040. The heliocentric legs are optimized using the procedure described in Section III, imposing a minimum Earth close-approach distance of $10R_\oplus = 63710$ km. The resulting transfer characteristics are summarized in Table 5.

The optimizer tends to select early departure epochs, confirming that a longer time available for the heliocentric transfer and for the post-impact propagation generally increases the achievable asteroid deviation. The results also indicate that the final deviation is not governed only by the required v_∞ magnitude at the switching surface, but also by the orbital characteristics of the target asteroid. The departure conditions reported in Table 5 define the target states to be matched by the Earth–Moon escape optimizer. In particular, the departure epoch fixes the orientation of the synodic system with respect to the inertial one at the patching time.

Table 5. Optimized heliocentric transfers.

Asteroid ID	**1**	**2**
Departure [dd/mm/yy]	26/02/36	14/12/35
Arrival [dd/mm/yy]	28/08/36	09/09/36
Required v_∞ [km/s]	3.9936	1.9288
Position angles θ, δ [°]	56.03, -6.91	-44.6, 2.78
$\boldsymbol{v}_\infty$ angles α, β [°]	61.81, -7.11	-20.52, -6.73
Deviation achieved [km]	63709.99	117229.09

Escape Results: Scenario 1. The escape performances for the first scenario are reported in Table 6. Overall, the two parking orbits exhibit comparable patching accuracy at the switching surface, with the resonant 2:1 orbit providing an almost perfect match in the position direction. The main difference is observed in the maneuvering cost as the 3:1 orbit requires nearly 300 m/s less total escape Δv_{tot}, mainly because the first maneuver is less expensive for this departure geometry. The time of flight is instead slightly more favorable for the 2:1 transfer, which reaches the switching surface about 1 day earlier. Fig. 3 and Fig. 4 show the optimized escape trajectories for both orbits in the rotating system.

The close Earth passage allows the optimizer to exploit the Oberth effect through the second maneuver, while the collision-avoidance constraint ensures that the trajectory remains outside the prescribed safety region. Although the optimization is performed in the full three-

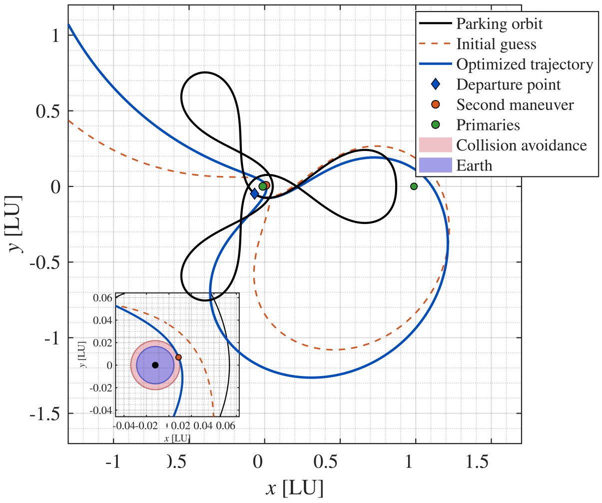

Fig. 3: *Escape trajectory for Resonant 3:1 to Asteroid 1.*

Table 6. Escape performances for resonant 3:1 and resonant 2:1 for scenario 1.

Scenario 1	$\boldsymbol{\Delta v_1}$ **[km/s]**	$\boldsymbol{\Delta v_2}$ **[km/s]**	$\boldsymbol{\Delta v_{tot}}$ **[km/s]**	**TOF[days]**	$\boldsymbol{v_\infty}$ **[km/s]**	$\boldsymbol{\delta_v}$ **[-]**	$\boldsymbol{\eta_r}$ **[°]**	$\boldsymbol{\eta_v}$ **[°]**
3:1	0.13756	0.81953	0.95709	21.40	3.95367	0.999%	1.6289	4.9965
2:1	0.45157	0.81793	1.26950	20.09	3.95367	0.999%	0.6161	4.9965

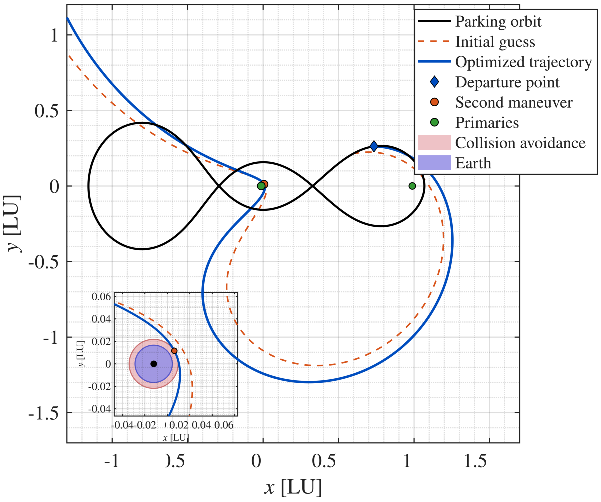

Fig. 4: *Escape trajectory for Resonant 2:1 to Asteroid 1*

dimensional space, the trajectories are shown as projections onto the $x - y$ plane for visualization purposes. This representation is appropriate for the present transfer, since the out-of-plane component remains small and does not significantly affect the interpretation of the escape geometry.

Escape Results: Scenario 2. The escape performances for the second scenario are reported in Table 7. The results are consistent with the trend observed in the previous case. The two parking orbits provide comparable patching accuracy at the switching surface, although the residual errors are slightly larger than in the first scenario. From a performance standpoint, the resonant 3:1 orbit again provides the most favorable solution, requiring a lower total escape Δv and a significantly shorter time of flight. As in the previous case, the difference in total maneuvering cost is mainly driven by the first impulse. Fig. 5 and Fig. 6 show the optimized escape trajectories for the scenario in the rotating system.

The patching conditions at the switching surface for the resonant 2:1 orbit are shown in Fig. 7. The small residuals between target and achieved states confirm the suitability of the proposed workflow for preliminary trajectory design. Only the patching-condition plot for the resonant 2:1 orbit is reported, since the corresponding 3:1 results exhibit the same qualitative behavior and would be visually repetitive.

Combining the stationkeeping results in Table 4 with the escape performances in Table 6 and Table 7 reveals a clear trade-off between storage and departure performance. The 3:1 orbit requires lower escape Δv_{tot} for the analyzed targets, but at the cost of a substantially higher annual stationkeeping requirement. This is especially relevant for a pre-deployed interceptor, since both the target and the waiting time before deployment are unknown a priori.

Since escape performance is target-dependent, the advantage observed for the 3:1 orbit cannot be generalized without a broader reachability analysis. For the present cases, however, a conservative estimate suggests that the 3:1 architecture remains preferable for storage durations

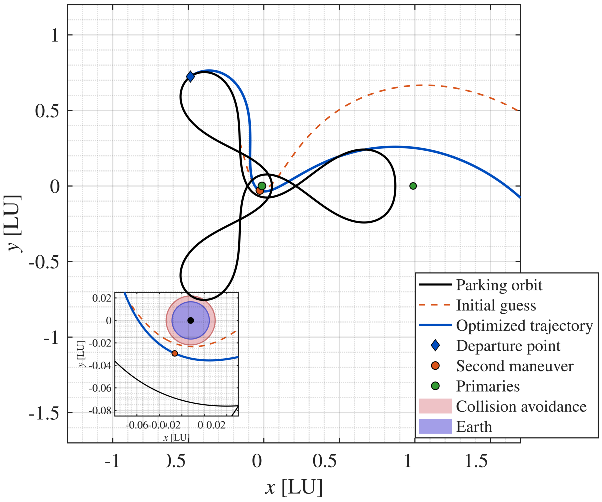

Fig. 5: *Escape trajectory for Resonant 3:1 to Asteroid 2*

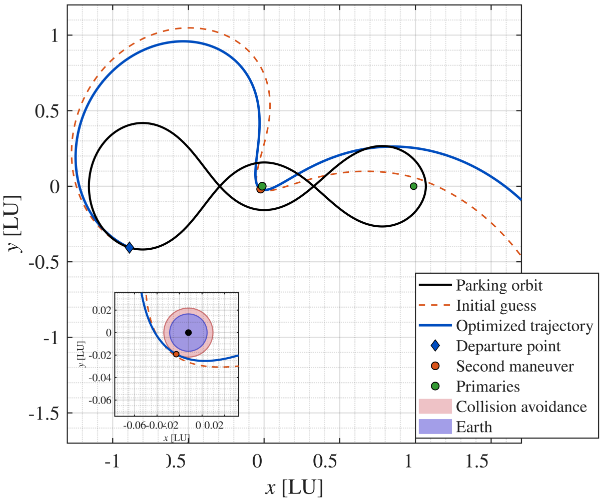

Fig. 6: *Escape trajectory for Resonant 2:1 to Asteroid 2*

Table 7. Escape performances for resonant 3:1 and resonant 2:1 for scenario 2.

Scenario 1	$\boldsymbol{\Delta v_1}$**[km/s]**	$\boldsymbol{\Delta v_2}$**[km/s]**	$\boldsymbol{\Delta v_{tot}}$**[km/s]**	**TOF[days]**	$\boldsymbol{v_\infty}$**[km/s]**	$\boldsymbol{\delta_v}$**[-]**	$\boldsymbol{\eta_r}$**[°]**	$\boldsymbol{\eta_v}$**[°]**
3:1	0.12901	0.32463	0.45364	15.81	1.90951	0.9999%	4.9999	4.9999
2:1	0.40247	0.23163	0.63410	22.98	1.90951	0.9998%	4.2311	4.9977

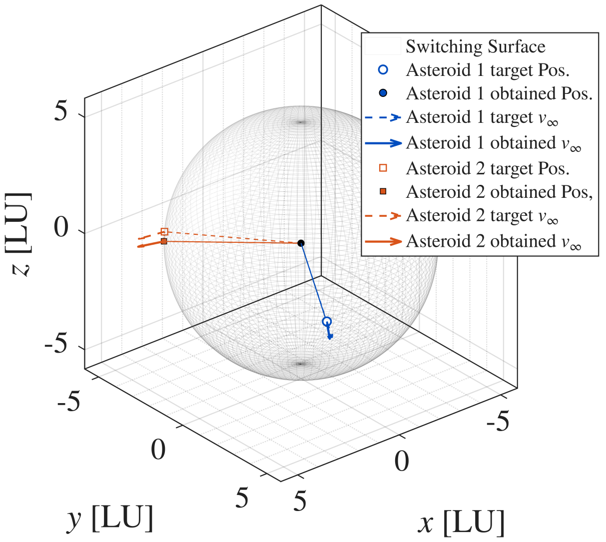

Fig. 7: *Patching conditions for Resonant 2:1.*

shorter than roughly 15-20 years, whereas the 2:1 orbit becomes more attractive for longer deployments due to its much lower maintenance cost.

Interception results. The results in Table 5 assume a spacecraft mass at impact of $m_{SC} = 2500$ kg, considered representative of a pre-deployed kinetic interceptor. While this mass is sufficient for the fictitious cases analyzed here, larger PHO-like asteroids may require substantially higher momentum transfer to achieve a safe deviation. A single heavier interceptor could provide this capability, but launching and maintaining such a spacecraft in the Earth-Moon environment may be impractical. A potential alternative is the use of multiple kinetic impactors, as investigated in [22]. By distributing the required momentum transfer among several lower-mass spacecraft, the cumulative deflection can be increased without relying on a single massive interceptor. This is illustrated in Fig. 8, which shows the total impactor mass required to obtain a fixed deviation of 10 Earth radii as a function of asteroid diameter. For an asteroid of about 140 m diameter, the required total mass is approximately 12000 kg for asteroid 1 trajectory, which could be achieved by a constellation of twelve 1000 kg impactors. It should be noted that this analysis assumes a fixed impact trajectory and an equivalent simultaneous momentum transfer. Optimizing the trajectory and impact conditions of each individual impactor could further improve the overall deflection efficiency and potentially reduce the required total interceptor mass.

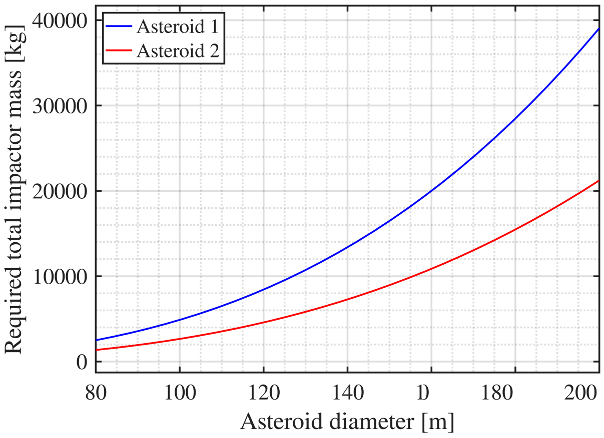

Fig. 8: *Impactor mass as a function of asteroid diameter.*

V. CONCLUSIONS

This work presents a preliminary design workflow for assessing candidate Earth–Moon parking orbits for pre-deployed kinetic impactors. Two representative resonant orbits, belonging to the 2:1 and 3:1 families, are selected to test the complete framework. The results highlight a trade-off between long-term storage capability and escape performance: the 2:1 orbit exhibits a significantly lower annual stationkeeping cost, whereas the 3:1 orbit achieves lower escape maneuvering costs for the two fictitious hazardous objects considered as test cases. This shows that orbit selection must be treated as a coupled design problem, rather than driven by storage efficiency or escape performance alone.

The results also support the viability of the proposed pre-deployed interceptor architecture. For the analyzed cases, the impactor achieves the required asteroid deviation with approximately five years of warning time, while the transfer to the asteroid takes only about seven to nine months. This indicates that a pre-deployed spacecraft could still provide interception capability for shorter-warning scenarios, although the final deviation depends on the available post-impact propagation time.

Among future developments, a first straightforward extension is to apply the proposed methodology to a broader set of orbit families and to multiple members within each family, in order to generalize the analysis beyond the two representative cases considered here. In addition, reachability maps should be constructed for each candidate orbit to quantify the accessible heliocentric departure conditions and provide a more complete assessment of the reachable target space.

On the escape side, the current bi-impulsive strategy could be expanded toward a larger design space, including natural escape mechanisms in higher-fidelity dynamical models and transfer strategies that exploit solar perturbations to reduce the departure cost.

Overall, the proposed workflow does not identify an absolute best parking orbit, but establishes a preliminary framework for comparing candidate Earth–Moon orbits in terms of stationkeeping cost, escape capability, and asteroid-deflection performance. This provides a basis for future systematic studies aimed at designing robust rapid-response architectures for planetary defense.

VI. REFERENCES

[1] David Morrison. *The Spaceguard survey: report of the NASA international near-Earth-object detection workshop*, volume 107979. NASA, 1992.

[2] D Perna, MA Barucci, and M Fulchignoni. The near-earth objects and their potential threat to our planet. *The Astronomy and Astrophysics Review*, 21(1):65, 2013.

[3] Tommy Grav, Amy K Mainzer, Joseph R Masiero, Dar W Dahlen, Tim Spahr, William F Bottke, and Frank J Masci. The neo surveyor near-earth asteroid known object model. *The Planetary Science Journal*, 4(12):228, 2023.

[4] R Terik Daly, Carolyn M Ernst, Olivier S Barnouin, Nancy L Chabot, Andrew S Rivkin, Andrew F Cheng, Elena Y Adams, Harrison F Agrusa, Elisabeth D Abel, Amy L Alford, et al. Successful kinetic impact into an asteroid for planetary defence. *Nature*, 616(7957):443–447, 2023.

[5] Claudio Maccone. Optimal trajectories from the earth-moon l1 and l3 points to deflect hazardous asteroids and comets. *Annals of the New York Academy of Sciences*, 1017(1):370–385, 2004.

[6] Andrea Pasquale. *Planetary defense and exploration mission design leveraging the Cislunar environment*. PhD thesis, Politecnico di Milano, 2022.

[7] Kaiduo Wang, Qi Zhou, Yandong Liu, Mingtao Li, and Yirui Wang. Research on space-based kinetic impactor disrupting small-sized asteroids under short warning time conditions. *Acta Astronautica*, 219:291–299, 2024.

[8] Joan Pau Sánchez, David Morante, Pablo Hermosin, Daniel Ranuschio, Alvaro Estalella, Dayana Viera, Simone Centuori, Geraint Jones, Colin Snodgrass, Anny Chantal Levasseur-Regourd, et al. Esa f-class comet interceptor: trajectory design to intercept a yet-to-be-discovered comet. *Acta Astronautica*, 188:265–277, 2021.

[9] Thomas A Pavlak. *Trajectory design and orbit maintenance strategies in multi-body dynamical regimes*. PhD thesis, Purdue University, 2013.

[10] Andrea Pasquale, Michele Lavagna, F Renk, et al. Cislunar escape trajectories through patched sun-earth/earth-moon three-body problem. In *International Astronautical Congress: IAC Proceedings*, pages 1–9, 2021.

[11] David A Vallado. *Fundamentals of astrodynamics and applications*, volume 12. Springer Science & Business Media, 2001.

[12] Victor Szebehely. *Theory of orbit: The restricted problem of three Bodies*. Elsevier, 2012.

[13] Daniel Grebow. Generating periodic orbits in the circular restricted three-body problem with applications to lunar south pole coverage. *MSAA Thesis, School of Aeronautics and Astronautics, Purdue University*, pages 8–14, 2006.

[14] Herbert B Keller. Constructive methods for bifurcation and nonlinear eigenvalue problems. In *Computing Methods in Applied Sciences and Engineering, 1977, I: Third International Symposium December 5–9, 1977*, pages 241–251. Springer, 2006.

[15] Gerard Gómez, Kathleen C Howell, Josep Masdemont, and Carles Simó. Station-keeping strategies for translunar libration point orbits. *Advances in Astronautical Sciences*, 99(2):949–967, 1998.

[16] Ariadna Farrés, Chen Gao, Josep J Masdemont, Gerard Gómez, David C Folta, and Cassandra Webster. Geometrical analysis of station-keeping strategies about libration point orbits. *Journal of Guidance, Control, and Dynamics*, 45(6), 2022.

[17] Hermann Oberth. *Ways to spaceflight*. Number 622. National Aeronautics and Space Administration, 1972.

[18] H. Sekine, K. Oguri, Y. Kawabata, and R. Funase. Robust trajectory design for earth-to-lunar orbit transfers via sequential convex programming. In *AAS Guidance, Navigation, and Control Conference*, Breckenridge, CO, 2026.

[19] Richard H. Battin. *An Introduction to the Mathematics and Methods of Astrodynamics*. AIAA Education Series. AIAA, revised edition, 1999.

[20] Kaisa Miettinen. *Nonlinear multiobjective optimization*, volume 12. Springer Science & Business Media, 1999.

[21] Andrew F Cheng, Harrison F Agrusa, Brent W Barbee, Alex J Meyer, Tony L Farnham, Sabina D Raducan, Derek C Richardson, Elisabetta Dotto, Angelo Zinzi, Vincenzo Della Corte, et al. Momentum transfer from the dart mission kinetic impact on asteroid dimorphos. *Nature*, 616:457–460, 2023.

[22] M. Fonseca Becker, K. Hernández Bandrich, A. Massini, N. May, S. Manoj Patwardhan, and A. Capannolo. Virtual thrust-based control formulation for multiple kinetic impactor asteroid deflection. In *30th International Symposium on Space Flight Dynamics*, Toulouse, France, 2026.